Magneto-optical control decoupled from the optical response in magnetic metallic gratings

Leyi Chen, Shuyu Xiao, Jinlong Gao, Zhixiong Tang, Shaolong Tang,* and Youwei Du

Collaborative Innovation Center of Advanced Microstructures, Jiangsu Key Laboratory for Nanotechnology, Nanjing National Laboratory of Microstructures and Department of Physics, Nanjing University, Nanjing 210093, China

(Received 19 October 2017; revised manuscript received 17 March 2019; published 27 March 2019)

Structured metallic and magnetic materials have attracted increasing attention due to their potential for label-free molecular detection, based on the control of the phase of light. Traditionally, tuning magneto-optical signals via magnetoplasmon leads to an excessively low light energy at the critical position in the spectrum. Thus, improving the reflectivity of magnetoplasmon-based photonic devices is a promising method to enhance their environmental adaptability. Here, we introduce a strategy for decoupling magneto-optical signal control and modulation of the reflection spectral line shape in ferromagnetic metallic gratings. This strategy is based on the sensibility of metallic gratings to the incident polarization state and the conclusion that the spin-orbit coupling induced orthogonal plasmon mode can be treated as from a pseudolight source. The decoupling and other phenomena of the oft-repeated magneto-optical Kerr rotation reversals and sensitivity to incident angle are validated using a cobalt grating.

DOI: 10.1103/PhysRevB.99.094437

I. INTRODUCTION

Plasmonics provides a delicate and efficient pathway to manipulate light-matter interaction at nanoscale by concentrating the electromagnetic energy of light in subwavelength area near the interface [1–3]. When plasmonic nanostructures contain magneto-optical active materials, an additional degree of freedom opens up to control the intensity and polarization of light on subnanosecond timescales via an external magnetic field [4–9]. Previous investigations have revealed that magneto-optical activity can be very effectively manipulated by introducing spatial confinement along the direction of the incident polarization in both nanoparticles [10–13] and periodic nanostructures [14–18], leading to various applications such as all-optical magnetic data storage [19], all-optical light isolators and modulators [20,21], and ultraprecise distance probe [22]. Specifically, with an elaborate design, the concerted action of plasmonics and magnetization can manipulate the sign of the rotation of the reflected light's polarization, producing magneto-optical Kerr rotation reversal [23]. This strategy can be used as an improved method to achieve ultrasensitive and label-free molecular-level detection [24].

The main disadvantage of magnetoplasmon-based photonic devices is that tuning light's polarization inevitably leads to a tremendous change in the line shape of the reflection/transmission spectrum due to the direct excitation of surface plasmons (SPs) [14–20]. In particular, the peak of the magneto-optical signal and the Kerr rotation reversal position usually correspond to the lowest light energy position in the spectrum [20,23–25]. This requirement of the wide energy dynamic range in high-precision detection is a huge obstacle for the applications of magneto-optical devices. Although many studies have attempted to obtain a large magneto-optical signal and reflectivity/transmissivity simultaneously [7,26–28], few have investigated the underlying physical mechanism that leads to the strong coupling between magneto-optical responses and spectral line shapes.

Here, we provide a route to independently control magneto-optical Kerr rotation that is decoupled from the modulation of the reflection spectrum. Utilizing the sensitivity of metallic gratings to the polarization state of incident light, the drastic impact of the nanostructures on the reflection spectrum is avoided. Meanwhile, the magneto-optical Kerr spectrum can still be manipulated. We elucidate the underlying mechanism proposed by Maccaferri *et al.*, that the orthogonal electron motion stemming from the spin-orbit coupling can be modulated by nanostructures, treated as if it were from a pseudolight source, and used to control the phase of light [29]. Obvious magneto-optical signal manipulation and reflectivity are obtained simultaneously using this radical approach.

In addition to obtaining consistently strong reflection over a very large wavelength range, the unmodulated reflection spectrum has other advantages. In a recent study, the polarization of light has been proposed as a potential information carrier in optical communications [30]. Therefore, the structure can be used as a photonic device to retain the spectrum information of the incident light while the polarization is changed by an external magnetic field. The fact that light can act as a dual signal carrier, the additional magneto-optical spectrum signal coexisting with the spectrum information inherited from the front device in the integrated photonic circuits, is very attractive.

II. RESULTS

A. Spin-orbit coupling induced dipoles

Our scheme is based on a magnetic metallic grating, which is shown in the inset of Fig. 1(a). For the sake of

*Corresponding author: tangsl@nju.edu.cn

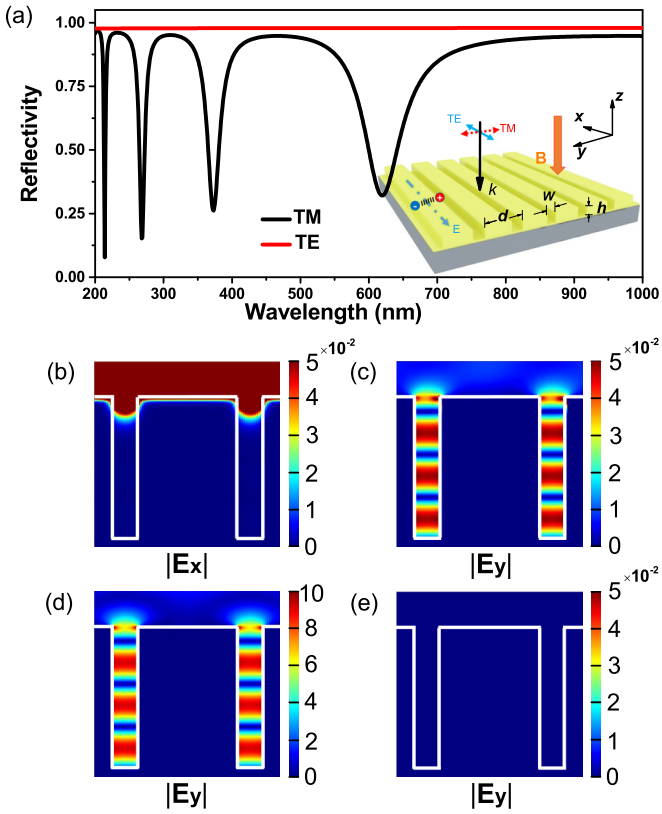

FIG. 1. Simulated reflectivity and field distribution of the IM grating model. (a) Simulated reflectivity under normal incident light. The TE-polarized light has the electric field of the incident light parallel to the x axis, and the transverse magnetic (TM)-polarized light is parallel to the y axis. Simulated field distribution of $|E_x|$ for the TE incident light (b), $|E_y|$ for the TE incident light (c), and $|E_y|$ for the TM incident light (d) for a 277-nm light source. (e) Simulated field distribution of $|E_y|$ for the TE-polarized 277-nm incident light with the permittivity tensor without off-diagonal elements.

clarity and universality, an artificial metal with its diagonal element of the permittivity tensor obeying the Drude model $\varepsilon = 1 - \omega_p^2/(\omega^2 + i\gamma\omega)$ is used in the finite-difference time-domain (FDTD) simulation. A small $\gamma = 0.49\,\text{eV}$ and an extraordinary large $\omega_p = 49.2\,\text{eV}$ are adopted to reduce the interference caused by the Ohmic losses and intrinsic light absorption of metals in the short wavelength region. A gyration $g = 0.016 - i0.0092$ is adopted to provide appreciable magneto-optical activity [20]. The artificial metal is named the ideal metal (IM).

The simple nanostructure of the metallic grating forms a wire-grid polarizer and its sensitivity to polarization has been extensively studied [31–35]. Typically, when the wavelength λ is greater than the period d, the metallic grating exhibits reflection similar to that of a flat surface for transverse electric (TE)-polarized light, i.e., the electric field is parallel to the grooves, as shown in the inset of Fig. 1(a). When the external polar magnetic field acts as a perturbation, the TE reflection spectrum remains nearly flat in Fig. 1(a). This phenomenon offers a route to retain the spectral information of incoming light when TE-polarized light is chosen as the source.

Positioned in the polar magnetic field, the permittivity tensor of a magneto-optical active material can be described as an antisymmetric matrix with $\varepsilon_{xx} \approx \varepsilon_{yy} \approx \varepsilon_{zz} \approx \varepsilon$ and $\varepsilon_{xy} = -\varepsilon_{yx} = -ig$, while the remaining elements are zero. That nanostructures can alter the field distribution near the interface can also be expressed as nanostructures turning the mixed layer composed of themselves and the filling materials into a uniform medium with a brand-new permittivity tensor. Thus, the permittivity tensor cannot directly describe the properties of the nanostructures.

When a subwavelength grating is impinged by normal TE-polarized light, the impact on the electrons within the grooves can be ignored. Figure 1(b) clearly shows that the incident TE light is blocked at the entrance of the groove. For the electrons at the ridge of the grating, driven by the electric field E_0 of the incident light, they collectively oscillate along the x direction, which is similar to what happens on a flat surface. In contrast, the electron motion component along the y direction is complicated. According to the study by Maccaferri *et al.*, spin-orbit coupling can be described through a second electric field [29]. The electrons gain momentum that is transferred from their movements along the x direction via spin-orbit interaction, leading to the electric polarization $P_y^0 = igE_0$. This behavior has the same result as if they were directly driven by a TM light with $E_y^0 = igE_0/(\varepsilon - \varepsilon_m)$ mathematically, where ε_m is the dielectric constant of the surrounding medium. It can be confirmed by the simulation results in Fig. 1. The field distribution along the y direction in Fig. 1(c) is just the same as that with actual TM-polarized incident light in Fig. 1(d). Figure 1(e) shows a vanishing $|E_y|$ when the permittivity tensor without off-diagonal elements in the simulation to certify that the field distribution in Fig. 1(c) originated from the off-diagonal elements, i.e., the spin-orbit coupling. Thus, the derived result is reasonable, and the spin-orbit coupling induced orthogonal electron motion can be treated as if it were driven by the pseudo-TM-polarized light.

Due to the spatial confinement of the grating along the y direction, most of the moving electrons are intercepted at the corner of the ridge, while positive charges appear at the other side. Consequently, an electric dipole $\mathbf{P}_r$ forms. Acting as a new light source, $\mathbf{P}_r$ emits wavelets with the same frequency as E_y^0. This process can be considered as Thomson scattering in the optical wavelength range [36,37]. If there is only one single nanowire, the polarization of the reflected light is determined by the far-field radiation of $\mathbf{P}_r$. When there is an array of grooves, another dipole $\mathbf{P}_a$ forms simultaneously at the groove opening, and the two dipoles are always opposite, as shown in Fig. 2. The contribution of the two dipoles to the magneto-optical signal is mainly influenced by two factors: whether the wavelets emitted from the dipoles can escape from the interface, and whether the presence of $\mathbf{P}_a$ affects the response of the oscillating electrons to the incident light, which mainly determines the sign of the Kerr rotation.

B. Decoupled polar magneto-optical Kerr rotation control

For $\mathbf{P}_r$, the wavelets emitted from two adjacent ridges have an optical path difference $\Delta S = d\sin\theta$, where θ is the emergence angle. For subwavelength gratings, the normal wavelets are in phase and thereby allow the far-field radiation.

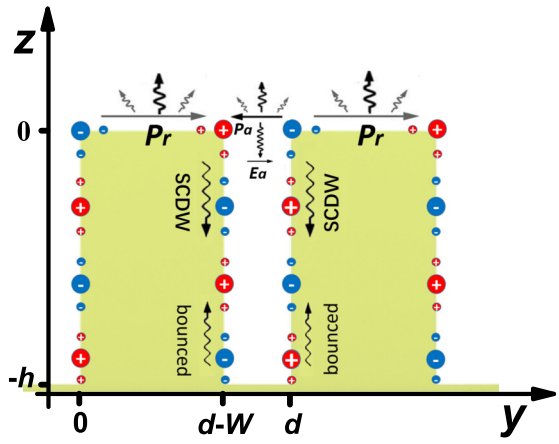

FIG. 2. Schematic of the spin-orbit coupling induced wavelet emission and the formation of the surface charge density waves (SCDWs) on the walls.

When $\theta \neq 0$, $\Delta S < d < \lambda$, none of the oblique wavelets can radiate to the far field because they are never in phase. All of the oblique wavelets form a nonsinusoidal standing wave, bounded at the interface between air and the grating [38]. The same conclusion can be drawn for $\mathbf{P}_a$: only normal wavelets can radiate to the far field, and contribute to Kerr rotation in the $\lambda > d$ range.

In addition to emitting wavelets towards $+z$, $\mathbf{P}_a$ simultaneously transmits wavelet $\mathbf{E}_a$ inside the grooves along $-z$. This wavelet drives electrons on the groove walls to oscillate. Thus, SCDWs are formed and propagate along $-z$ [37,38]. If the SCDWs can reach the bottom of the grating before being completely absorbed, a bounced wave will appear, as sketched in Fig. 2. Standing waves are formed with the metal-covered bottom as the node. As the wavelength increases, the nodes and antinodes alternately become located at the groove opening, as shown in Fig. 3(c). When the opening moves across the node, the surface charge vanishes on the top of the grating, leading to the emission of an invisible wavelet for both $\mathbf{P}_r$ and $\mathbf{P}_a$, which act as dim SCDWs on the walls. When the antinode moves to the opening (at 214, 268, 373, and 620 nm), the electrons are most concentrated at the corners and excite strong SCDWs. The TE reflection spectrum in Fig. 3(a) remains flat because it is decoupled from the magneto-optical signal control. Orthogonal electron motion can be treated as if it were driven by the pseudo-TM-polarized light. Thus, the TM reflection spectrum in Fig. 3(a) can be used to identify the corresponding wavelength at which the antinode meets the opening. The relation between the wavelength λ and the depth h of the groove should be $\lambda = 4h/(2n-1)$ corresponding to Fabry-Perot resonance, when the nth antinode meets the opening. However, an obvious redshift is observed. The inset in Fig. 3(c) shows that the wavelength of the SCDWs is 195 nm for 214-nm incident light, displaying the subwavelength characteristic, which is the main reason for the observed redshift. The phase anomaly of the SCDWs near the opening, at $Z = 0$ in the inset in Fig. 3(c), also plays an important role.

The pseudolocalized plasmon resonance (PLPR) assisted dipole oscillator model is set up to describe the motion of the free electrons along the y direction on the grating ridge.

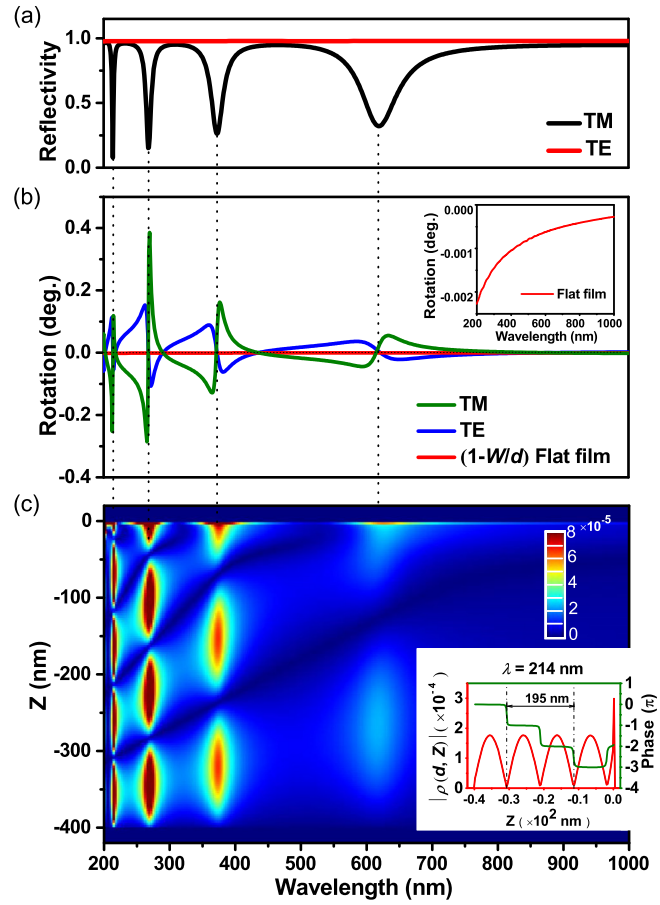

FIG. 3. Modulated polar Kerr rotation and surface charge density on the grating wall. (a) Simulated reflectivity of the IM grating under normal incident light. Every dip in the spectrum corresponds to an antinode of the SCDW standing wave. (b) Simulated polar Kerr rotation of the IM grating, compared with the result obtained for a 50-nm-thick IM flat film amended by the area fraction. The inset shows a magnification of the IM film. (c) Simulated surface charge density $|\rho|$ on the wall of the grating (d and z are sketched in Fig. 2), showing the intensity change of the SCDWs. The number of bright specks corresponds to n. The inset shows the surface charge density and phase along the z axis for the 214-nm incident light.

Every antinode of the SCWDs causes a charge accumulation on the ridge of the grating similar to the excitation of localized plasmon resonance (LPR), as shown in Fig. 1(c), which can be vividly called PLPR. A series of PLPRs appear to be excited on the spectrum due to the standing waves. Thus the displacement u of the free electron is governed by an equation of motion in the form

$$m_0\frac{d^2u}{dt^2} + m_0\gamma\frac{du}{dt} + m_0\omega_i^2 u = -eE_y^0 \text{ for } \omega_i - \Delta\omega_i \leqslant \omega \leqslant \omega_i + \Delta\omega_i, \quad (1)$$

where γ is the frictional force modeled damping rate, and e is the magnitude of the electric charge of the electron. The physical picture is described as follows. A battery of discrete ω_i are scattered on the spectrum. Every ω_i corresponds to a wavelength at which an antinode meets the opening, i.e., the excitation position of PLPR. When the frequency of the

incident light sweeps near a certain ω_i, the relevant restoring force term is activated due to the charge accumulation at the corners caused by the excitation of PLPRs. The polarization is given by

$$P_y^a = -Neu = \frac{Ne^2}{m_0}\frac{1}{\omega_i^2 - \omega^2 - i\gamma\omega}E_y^0, \tag{2}$$

where N is the number of electrons per unit volume. In the case of meeting nodes, the PLPRs are not excited. With the absence of charge accumulation, Eq. (1) can be simplified to

$$m_0\frac{d^2u}{dt^2} + m_0\gamma\frac{du}{dt} = -eE_y^0, \tag{3}$$

which has the same form as the Drude model. Thus, the grating can be considered to exhibit Kerr rotation similar to that of a flat film. From Eq. (3), we obtain the polarization

$$P_y^n = -Neu = -\frac{Ne^2}{m_0}\frac{1}{\omega^2 + i\gamma\omega}E_y^0. \tag{4}$$

Comparing Eqs. (2) and (4) reveals that PLPRs bring a modified factor $\alpha = (\omega^2 + i\gamma\omega)/(\omega^2 + i\gamma\omega - \omega_i^2)$. Then, around the antinodes, the wavelets are emitted to the far field, giving rise to Kerr rotation θ_k^a, which is formulated as

$$\theta_k^a = f\mathrm{Re}\left(\frac{\eta P_y^a}{P_x}\right) = f\mathrm{Re}\left(\frac{\eta\alpha P_y^n}{P_x}\right) = f\frac{\eta|\alpha||P_y^n|}{|P_x|}\mathrm{Re}(e^{i(\Delta\varphi+\varphi_a)})$$
$$= \eta|\alpha|f\frac{|P_y^n|}{|P_x|}\cos(\Delta\varphi + \varphi_a), \tag{5}$$

where η is the real factor due to the wavelets from $\mathbf{P}_r$ and $\mathbf{P}_a$ canceling each other out, f is the area fraction $f = (d - W)/d$. The emergence of α introduces an amplitude modulation factor $|\alpha|$ and an additional phase shift $\varphi_a = \arctan[\mathrm{Im}(\alpha)/\mathrm{Re}(\alpha)]$ to the intrinsic phase difference $\Delta\varphi$ (determined by the intrinsic property of the material). As a result, the magneto-optical Kerr rotation is enhanced and reversed near every ω_i. The positions of the Kerr reversals are closely related to the value of $(\Delta\varphi + \varphi_a)$. The corresponding simulation results are shown in Fig. 3(b). When TE-polarized light is chosen as the source, various controls, including the enhancement and reversals of magneto-optical Kerr rotation signals, are regularly realized near every position where an antinode meets the opening; the undisturbed reflection spectrum is shown in Fig. 3(a). As a reference, the Kerr rotation spectrum for TM light is also presented.

To validate the proposed scheme, we fabricated a cobalt grating sample on a silicic substrate using interference lithography and dc magnetron sputtering, with the following dimensions: period $d = 380$ nm, depth of the grating $h = 200$ nm and slit width $W = 200$ nm. The topography of the regular grating structure is shown in Fig. 4(a). The measured and simulated reflection spectra using the TE and TM light source are plotted in Fig. 4(b). The TE reflection spectrum shows a flat line shape when $\lambda > d$, similar to that obtained from the cobalt flat film, showing the properties of the wire-grid polarizer, while the TM reflection spectrum used for comparison clearly shows the modulation of the incident light, as in previous studies [14–20]. In the TM reflection spectrum, the dips at 935 and 405 nm correspond to the Fabry-Perot resonances, or what we call "PLPRs", when $n = 1, 2$ in

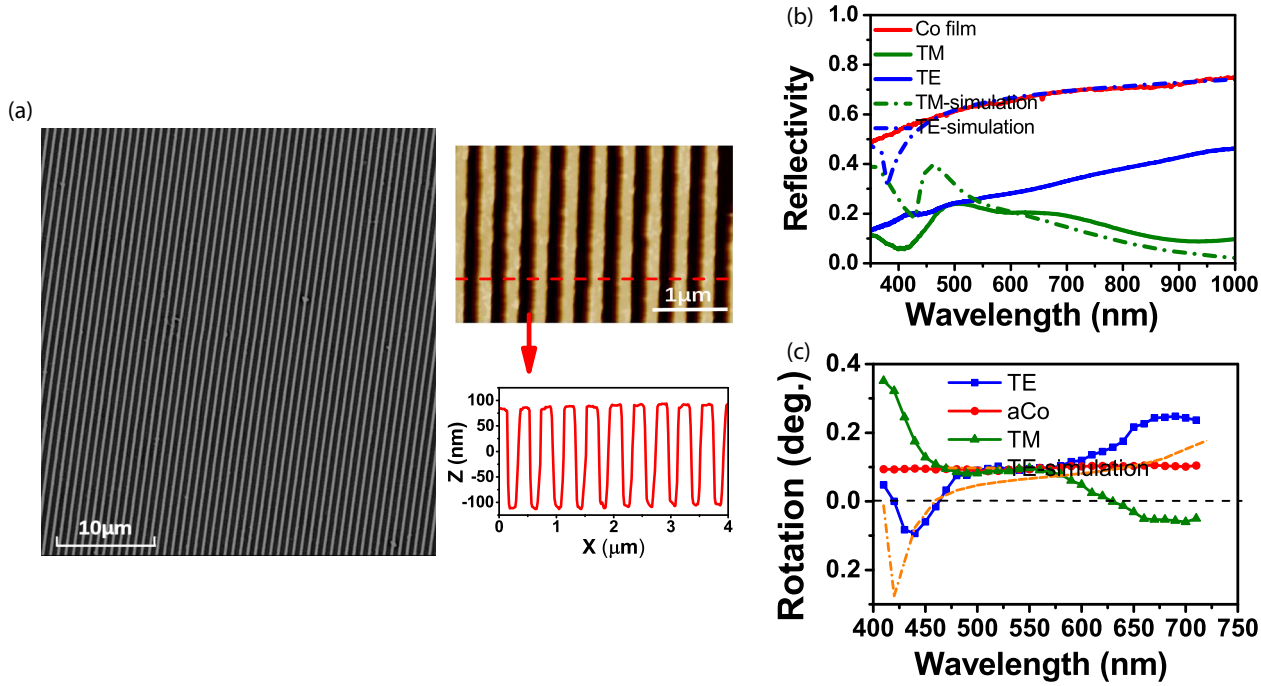

FIG. 4. Measured and simulated reflectivity and polar Kerr rotation of the Co grating. (a) Scanning electron microscopy and scanning probe microscopy images of the cobalt grating. (b) Reflectivity of the cobalt grating for normal incident light with both TE and TM polarization, compared with the result obtained for a 50-nm-thick flat cobalt film using normal TE-polarized incident light. (c) Polar Kerr rotation of the cobalt grating for both TE and TM polarization, compared with that of a 50-nm-thick flat cobalt film amended by the area fraction.

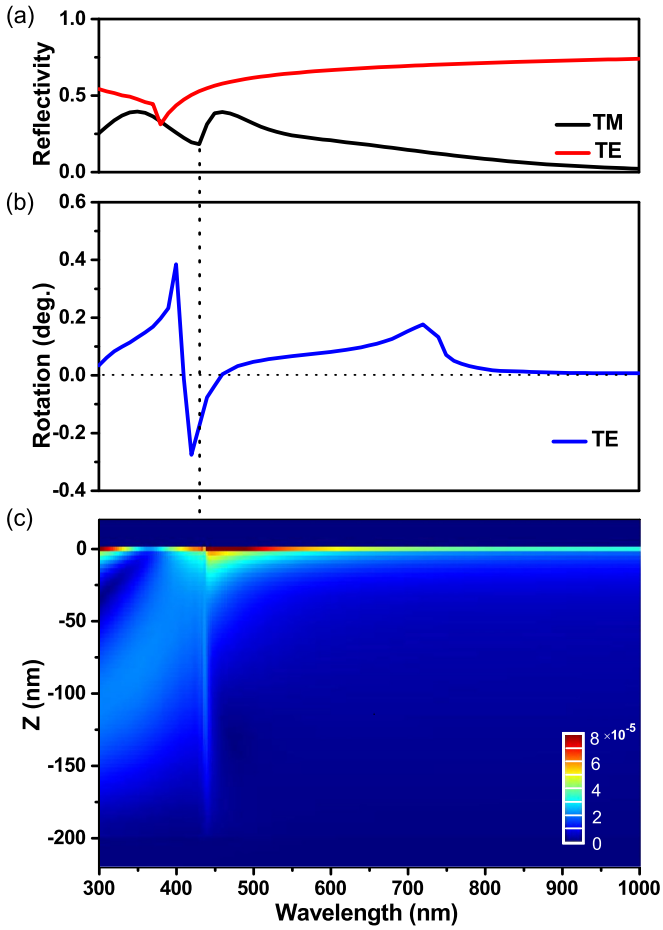

FIG. 5. Modulated polar Kerr rotation and surface charge density on the grating wall. (a) Simulated reflectivity of the Co grating sample under normal TM and TE incident light. (b) Simulated polar Kerr rotation of the Co grating sample. (c) Simulated surface charge density $|\rho|$ on the wall of the grating sample.

$\lambda = 4h/(2n-1) + \Delta_n$, where Δ_n is the redshift, which varies with d, W, h, and ε_m. The node of the SCDWs appears at approximately 500 nm, where the reflectivity is almost coincident with that observed for TE light. Consistent with the conclusion mentioned above, it mirrors the behavior of the wavelets from the spin-orbit coupling induced dipoles for the TE light. The magneto-optical Kerr rotation in Fig. 4(c) reverses twice for the TE light at 420 and 463 nm under the influence of the PLPR at 405 nm. In addition, clear enhancement occurs near 690 nm, compared with that in the area fraction-amended Co film (aCo). At approximately 500 nm, when the node meets the opening, the magneto-optical signal of the grating is the same as that of aCo, good agreement with the conclusion drawn based on Eq. (3). These verify the effective control of magneto-optical signals resulting from the influence of the SCDWs, based on the decoupling from the reflection spectrum. For reference, the simulated TE and TM reflection spectra using a realistic permittivity tensor of Co and realistic geometric parameters of the experimental grating sample are presented in Fig. 5, and the section corresponding to the experiment is specially cut and presented in Figs. 4(b) and 4(c). Compared with Fig. 3, it is easy to find similar results and the conclusion we get from Fig. 3 in Fig. 5, which indicates that our simulation results for the IM grating model reflect a universal conclusion. However, because of the limitation of grating depth and Ohmic losses of Co, the SCDWs on the grating wall cannot present the clear shape of a standing wave. But the effect of the charge accumulation on the ridge of the grating is obvious in Fig. 5(c). If the surface of the magnetic metal grating can be modified to reduce Ohmic losses, more significant and accurate manipulation to the magneto-optical Kerr spectrum can be achieved.

C. Extending to the longitudinal Kerr effect

Regarding the longitudinal magneto-optical Kerr effect, positioned in the magnetic field sketched in Fig. 6(a), the nonzero off-diagonal elements of the permittivity tensor should be described as $\varepsilon_{yz} = -\varepsilon_{zy} = ig$. For oblique incident light with its polarized direction in the plane of the light path, an electric dipole $\mathbf{P}_r$ forms because of the electric polarization $p_y = igE_z$ on the ridge, similar to the polar configuration mentioned above. In addition to the expected intensity change of the SCDW on the groove wall, charge accumulation always occurs at the opening of the groove but is less strongly related to the incident wavelength, as shown in the simulation result in Fig. 6(b), which differs significantly from Fig. 3(c). This phenomenon is attributed to the difference between the polar configuration and the longitudinal configuration. The wavefront of the oblique incident light reaches the grating/air interface with a phase difference along the x direction. This difference leads to a phase difference in the movements of electrons at different x positions, resulting in the out-of-step accumulation of the charges at the corner of the grating ridge. An additional simulation was performed to show the y component of the electric field at the corner in Fig. 6(d). Three peaks of $|E_y|$ are observed, all of which correspond to the excitation wavelengths in Fig. 6(b) (204, 246, and 305 nm). Thus, the electric field from the extra accumulation of positive and negative charges at the opening is constrained in the x direction and lacks a conspicuous y component. Therefore, the extra charge accumulation cannot make an additional contribution to the magneto-optical effect. Therefore, the mechanism found for the polar configuration can be extended to the longitudinal configuration.

Comparing Figs. 6(b) and 6(c) reveals that all three wavelengths corresponding to strong standing waves show a blueshift, as the incident angle increases from 45° to 50°. To explain this blueshift, the spatial distribution of surface charge density on the groove wall was simulated using 204-nm incident light. This simulation clearly shows the phase difference of the SCDW propagating along the $-z$ direction at different x position in Fig. 6(e). The equiphase surface of the SCDW is no longer parallel to the grating/air interface. In other words, the direction of the SCDW makes an angle with the z axis, as indicated by the black arrow in Fig. 6(e). From the geometric relationship, the distance between two adjacent equiphase positions along the $-z$ direction can be expressed as

$$\lambda_{\text{eff}} = \frac{\lambda \cdot \lambda_{\text{SCDW}}}{\sqrt{\lambda^2 - \lambda_{\text{SCDW}}{}^2 \cdot \sin^2\theta}}, \tag{6}$$

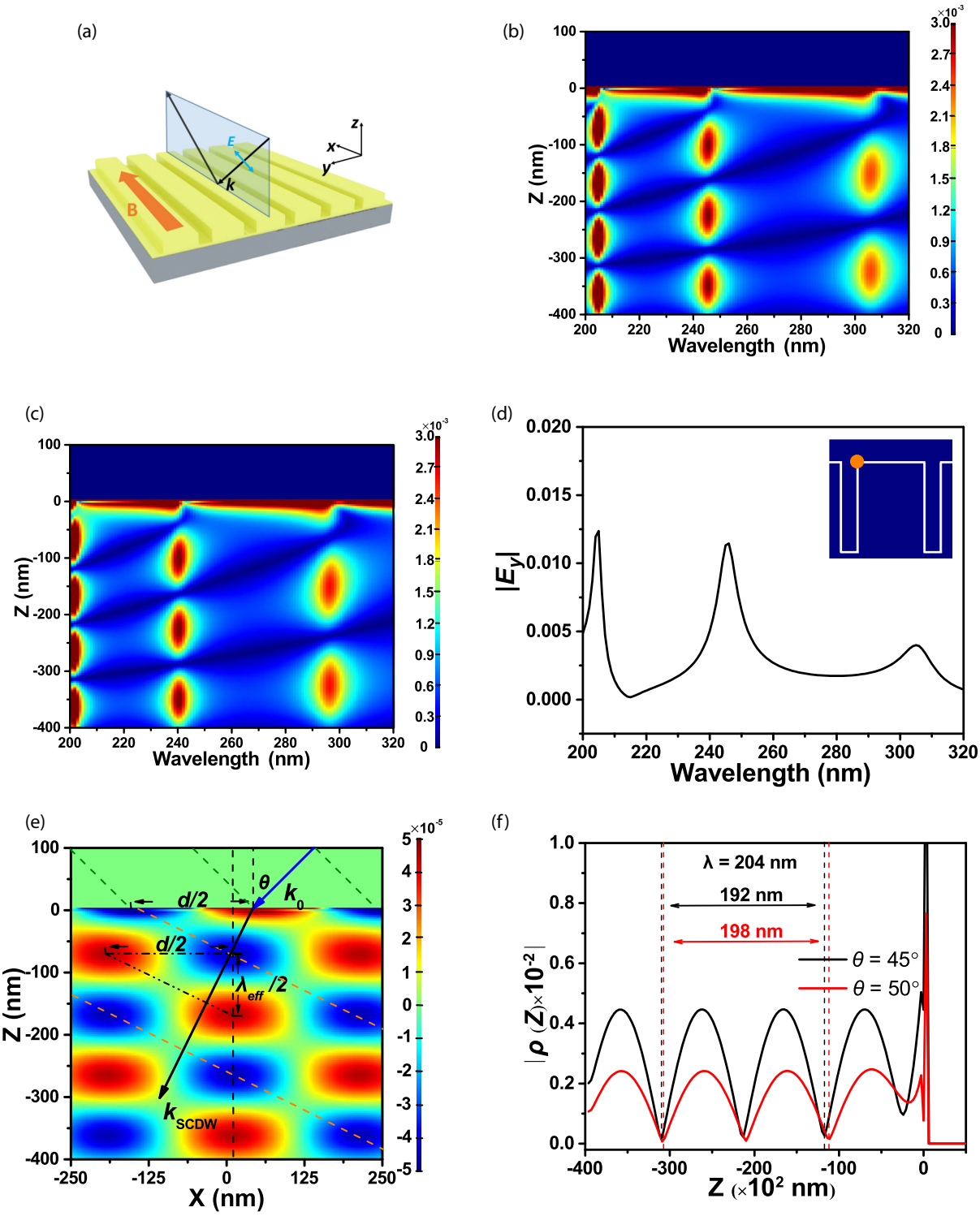

FIG. 6. Surface charge density distribution of the grating wall in the longitudinal configuration. (a) Schematic of the longitudinal magneto-optical Kerr configuration. The electric field of the incident light is in the plane of the light path. Simulated surface charge density $|\rho|$ on the wall of the grating at incident angles of 45° (b) and 50° (c) in the configuration in (a). (d) Simulated field distribution $|E_y|$ at the corner of the grating. The inset visualizes the simulated position. (e) Simulated spatial distribution of surface charge density on the wall at an incident angle of 45°. (f) Simulated surface charge density distribution along the $-z$ direction for 204-nm light at different incident angles.

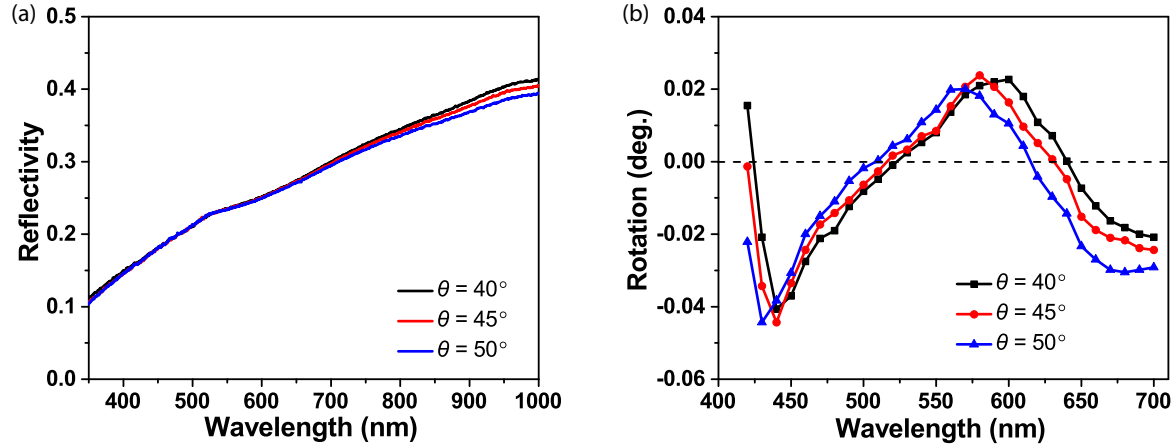

FIG. 7. Measured reflectivity and longitudinal Kerr rotation of the Co grating. (a) Measured reflectivity of the cobalt grating at different incident angles in the longitudinal configuration shown in Fig. 6(a). (b) Measured longitudinal Kerr rotation of the cobalt grating at different incident angles in the longitudinal configuration shown in Fig. 6(a).

where θ is the incident angle, λ is the incident wavelength, and λ_{SCDW} is the wavelength of the SCWD determined by the incident wavelength and the materials of the interface. λ_{eff} is defined as the effective wavelength of the SCDW, which actually determines the intensity of the SCDWs on the groove walls and the charge accumulation on the topside of the grating. According to Eq. (6), λ_{eff} increases as the incident angle θ increases. This conclusion can be seen more intuitively in Fig. 6(f). The distance between two adjacent equiphase position increases from 192 to198 nm, when the incident angle of the 204-nm light increases from 45° to 50°. Therefore, to obtain the same λ_{eff} and, thus, exert the same effect on the charge accumulation, a large incident angle must be combined with a shorter wavelength. This is the reason for the blueshift. The blueshift will eventually be reflected in the magneto-optical Kerr spectrum.

We characterized the reflection spectrum and the magneto-optical Kerr spectrum of the fabricated cobalt grating in the longitudinal configuration, as sketched in Fig. 6(a). The reflection spectrum in Fig. 7(a) shows a smooth rising curve and is not modulated by the nanostructure as commonly observed in previous studies [14–20]. Furthermore, it changes only slightly and remains almost coincident in the visible region as the incident angle increases from 40° to 50°. Correspondingly, the magneto-optical Kerr spectrum is clearly modulated and shows the expected blueshift in Fig. 7(b). The reversal of the sign of Kerr rotation occurs repeatedly at 420, 515, and 630 nm ($\theta = 45°$). The reverse positions can be modulated by the incident angle, which enriches the means of manipulating the profile of the magneto-optical spectrum. More subtly, the modulation range gradually enlarges as the wavelength increases when changing the same incident angle, from 15 nm near 515 nm to 24 nm near 630 nm. This behavior is qualitatively consistent with that observed by comparing Figs. 6(b) and 6(c).

III. CONCLUSION

In summary, we linked the polarization selectivity of metallic gratings to the fabrication of magneto-plasmonic nanostructures to realize the decoupling of the magneto-optical signal control and the modulation of reflectivity in both polar and longitudinal configurations. Both configurations obey the relationship $(E \cdot \Lambda) = 0$ between the electric field E of the incident light and the lattice vector Λ of the grating, which is traditionally considered to fail to meet the necessary conditions for SPs excitation in grating systems [19]. Here, we utilized this mismatch to avoid any dramatic impact on the reflection spectrum. Furthermore, we generalized the two orthogonal damped harmonic oscillators model in ferromagnetic nanodisk proposed by Maccaferri *et al.*, elucidating that the spin-orbit coupling induced electric field can be treated as if it were from a pseudo source, and can be variously altered by nanostructures similar to the real light source and even excite SPs in the orthogonal direction. This phenomenon provides a basis for achieving independent control of the magneto-optical effect in one-dimensional nanostructures. The consistently strong reflection we obtained via our radically improved alternative route covers a wide wavelength region instead of one or several wavelength positions, as described previously [7,26–28]. Additionally, developing a magnetoplasmon-based dual optical signal carrying technology is possible. We proposed that PLPR arises from the standing waves and leads to charge accumulation similar to that observed for classical LPR. For the magneto-optical effect, PLPRs have the same functionality to manipulate the sign of Kerr rotation. They can be excited repeatedly with sufficiently deep grooves, leading to an array of Kerr reversals that covers a wide band, which has broader potential applications in wide-range and multichannel high-sensitivity detection. Furthermore, in the longitudinal configuration, the incident angle provides an extra degree of freedom of manipulation, and the installation of the magnetic field is more conducive to the two-dimensionalization and miniaturization of optical devices.

ACKNOWLEDGMENTS

This work was supported by National Natural Science Foundation of China (NSFC) (11374146), Project funded by

China Postdoctoral Science Foundation (2018M632278), and the Jiangsu Planned Projects for Postdoctoral Research Funds (1701092C).

APPENDIX: METHOD

1. Optical and magneto-optical measurements

The optical reflectivity was measured using a white-light angle-resolved spectroscopy system (Idea Optics Co.) at different incident angles with TE and TM polarization separately. The light was focused on the sample into a spot with a diameter of approximately 1 mm.

For the magneto-optical measurements, we used a homemade magneto-optical Kerr system consisting of a wavelength-tunable pulsed laser working in the range of 410–710 nm. The light spot diameter was approximately 1 mm. Glan-Taylor prisms were used as the polarizer and analyzer. In the polar configuration, the light propagated to the sample surface with an incident angle of less than 1°, and an electromagnet was applied to provide a polar magnetic field up of to 15 kOe. In the longitudinal configuration, the incident angle was varied between 40°and 50°, and the magnetic field was as high as 2 kOe. The overall angle resolution of the system was below 0.001°.

2. Numerical simulation

The simulations of the optical reflectivity, the distribution of electric field intensity, the surface charge density, and the magneto-optical Kerr rotation were conducted using the finite-difference time-domain method.

In the simulation of the ideal metal grating model in Figs. 1, 3 and 5, the geometry of the calculation model is sketched in Fig. 2. The geometric parameters are $d = 200$ nm, $W = 40$ nm and $h = 400$ nm. The thickness of the cobalt bottom layer was set as 50 nm. The permittivity tensor of the IM in the simulation was stated previously.

In the simulation of the cobalt grating sample we characterized in Fig. 4, the geometric parameters are the same as the sample: period $d = 380$ nm, depth of the grating $h = 200$ nm, and slit width $W = 200$ nm. The index of the environment surrounding the grating is set as 1.15. The permittivity tensor of cobalt comes from Refractive index database [39] and Krinchik's results [40].

[1] A. Polman, Plasmonics applied, Science **322**, 868 (2008).

[2] J. Heber, Surfing the wave, Nature (London) **461**, 720 (2009).

[3] J. A. Schuller, E. S. Barnard, W. Cai, Y. C. Jun, J. S. White, and M. L. Brongersma, Plasmonics for extreme light concentration and manipulation, Nat. Mater. **9**, 193 (2010).

[4] V. V. Temnov, G. Armelles, U. Woggon, D. Guzatov, A. Cebollada, A. Garcia-Martin, J. Garcia-Martin, Tim Thomay, A. Leitenstorfer, and R. Bratschitsch, Active magneto-plasmonics in hybrid metal–ferromagnet structures, Nat. Photonics **4**, 107 (2010).

[5] D. J. Bergman and Y. M. Strelniker, Anisotropic ac Electrical Permittivity of a Periodic Metal-Dielectric Composite film in a Strong Magnetic Field, Phys. Rev. Lett. **80**, 857 (1998).

[6] M. Liu and X. Zhang, Plasmon-boosted magneto-optics, Nat. Photonics **7**, 429 (2013).

[7] V. I. Belotelov, L. L. Doskolovich, and A. K. Zvezdin, Extraordinary Magneto-Optical Effects and Transmission Through Metal-Dielectric Plasmonic Systems, Phys. Rev. Lett. **98**, 077401 (2007).

[8] V. L. Krutyanskiy, A. L. Chekhov, V. A. Ketsko, A. I. Stognij, and T. V. Murzina, Giant nonlinear magneto-optical response of magnetoplasmonic crystals, Phys. Rev. B **91**, 121411(R) (2015).

[9] B. Caballero, A. García-Martín, and J. C. Cuevas, Hybrid magnetoplasmonic crystals boost the performance of nanohole arrays as plasmonic sensors, ACS Photon. **3**, 203 (2016).

[10] J. Chen, P. Albella, Z. Pirzadeh, P. Alonso-GonzálezJ, F. Huth, S. Bonetti, V. Bonanni, J. Åkerman, J. Nogués, P. Vavassori, A. Dmitriev, J. Aizpurua, and R. Hillenbrand, Plasmonic nickel nanoantennas, Small **7**, 2341 (2011).

[11] Y. Liu, S. Palomba, Y. Park, T. Zentgraf, X. Yin, and X. Zhang, Compact magnetic antennas for directional excitation of surface plasmons, Nano Lett. **12**, 4853 (2012).

[12] J. L. Menéndez, B. Bescós, G. Armelles, R. Serna, J. Gonzalo, R. Doole, A. K. Petford-Long, and M. I. Alonso, Optical and magneto-optical properties of Fe nanoparticles, Phys. Rev. B **65**, 205413 (2002).

[13] C. Clavero, G. Armelles, J. Margueritat, J. Gonzalo, M. García del Muro, A. Labarta, and X. Batlle, Interface effects in the magneto-optical properties of Co nanoparticles in dielectric matrix, Appl. Phys. Lett. **90**, 182506 (2007).

[14] D. Floess, M. Hentschel, T. Weiss, H.-U. Habermeier, J. Jiao, S. G. Tikhodeev, and H. Giessen, Plasmonic Analog of Electromagnetically Induced Absorption leads to Giant Thin Film Faraday Rotation of 14°, Phys. Rev. X **7**, 021048 (2017).

[15] E. Th. Papaioannou, V. Kapaklis, P. Patoka, M. Giersig, P. Fumagalli, A. Garcia-Martin, E. Ferreiro-Vila, and G. Ctistis, Magneto-optic enhancement and magnetic properties in Fe antidot films with hexagonal symmetry, Phys. Rev. B **81**, 054424 (2010).

[16] M. V. Sapozhnikov, S. A. Gusev, V. V. Rogov, O. L. Ermolaeva, B. B. Troitskii, L. V. Khokhlova, and D. A. Smirnov, Magnetic and optical properties of nanocorrugated Co films, Appl. Phys. Lett. **96**, 122507 (2010).

[17] M. Rollinger P. Thielen, E. Melander, E. Östman, V. Kapaklis, B. Obry, M. Cinchetti, A. García-Martín, M. Aeschlimann, and E. Th. Papaioannou, Light localization and magneto-optic enhancement in Ni antidot array, Nano Lett. **16**, 2432 (2016).

[18] M. Kataja, T. K. Hakala, A. Julku, M. J. Huttunen, S. van Dijken, and P. Torima, Surface lattice resonances and magneto-optical response in magnetic nanoparticle arrays, Nat. Commun. **6**, 7072 (2015).

[19] V. I. Belotelov, I. A. Akimov, M. Pohl, V. A. Kotov, S. Kasture, A. S. Vengurlekar, A. V. Gopal, D. R. Yakovlev, A. K. Zvezdin, and M. Bayer, Enhanced magneto-optical effects in magnetoplasmonic crystals, Nat. Nanotechnol. **6**, 370 (2011).

[20] J. Y. Chin, T. Steinle, T. Wehlus, D. Dregely, T. Weiss, V. I. Belotelov, B. Stritzker, and Harald Giessen, Nonreciprocal plasmonics enables giant enhancement of thin-film Faraday rotation, Nat. Commun. **4**, 1599 (2013).

[21] V. I. Belotelov, L. E. Kreilkamp, I. A. Akimov, A. N. Kalish, D. A. Bykov, S. Kasture, V. J. Yallapragada, A. V. Gopal, A. M. Grishin, S. I. Khartsev, M. Nur-E-Alam, M. Vasiliev, L. L. Doskolovich, D. R. Yakovlev, K. Alameh, A. K. Zvezdin, and M. Bayer, Plasmon-mediated magneto-optical transparency, Nat. Commun. **4**, 2128 (2013).

[22] I. Zubritskaya, K. Lodewijks, N. Maccaferri, A. Mekonnen, R. K. Dumas, J. Åkerman, P. Vavassori, and A. Dmitriev, Active magnetoplasmonic ruler, Nano Lett. **15**, 3204 (2015).

[23] V. Bonanni, S. Bonetti, T. Pakizeh, Z. Pirzadeh, J. Chen, J. Nogués, P. Vavassori, R. Hillenbrand, J. Åkerman, and A. Dmitriev, Designer magnetoplasmonics with nickel nanoferromagnets, Nano Lett. **11**, 5333 (2011).

[24] N. Maccaferri, K. E. Gregorczyk, T. V. A. G. de Oliveira, M. Kataja, S. van Dijken, Z. Pirzadeh, A. Dmitriev, J. Åkerman, M. Knez, and P. Vavassori, Ultrasensitive and label-free molecular-level detection enabled by light phase control in magnetoplasmonic nanoantennas, Nat. Commun. **6**, 6150 (2015).

[25] L. Chen, J. Gao, W. Xia, S. Zhang, S. Tang, W. Zhang, D. Li, X. Wu, and Y. Du, Tunable Fano resonance and magneto-optical response in magnetoplasmonic structure fabricated by pure ferromagnetic metals, Phys. Rev. B **93**, 214411 (2016).

[26] C. Lei, L. Chen, Z. Tang, D. Li, Z. Cheng, S. Tang, and Y. Du, Enhancement of magneto-optical Faraday effects and extraordinary optical transmission in a tri-layer structure with rectangular annular arrays, Opt. Lett. **41**, 729 (2016).

[27] A. B. Khanikaev, A. V. Baryshev, A. A. Fedyanin, A. B. Granovsky, and M. Inoue, Anomalous Faraday effect of a system with extraordinary optical transmittance, Opt. Express **15**, 6612 (2007).

[28] V. Dmitriev, F. Paixão, and M. Kawakatsu, Enhancement of Faraday and Kerr rotations in three-layer heterostructure with extraordinary optical transmission effect, Opt. Lett. **38**, 1052 (2013).

[29] N. Maccaferri, A. Berger, S. Bonetti, V. Bonanni, M. Kataja, Q. H. Qin, S. van Dijken, Z. Pirzadeh, A. Dmitriev, J. Nogués, J. Åkerman, and P. Vavassori, Tuning the Magneto-Optical Response of Nanosize Ferromagnetic Ni Disks Using the Phase of Localized Plasmons, Phys. Rev. Lett. **111**, 167401 (2013).

[30] K. Lodewijks, N. Maccaferri, T. Pakizeh, R. K. Dumas, I. Zubritskaya, J. Åkerman, P. Vavassori, and A. Dmitriev, Magnetoplasmonic design rules for active magneto-optics, Nano Lett. **14**, 7207 (2014).

[31] E. Hecht, *Optics*, 3rd ed. (Addison-Wesley Longman, New York, 1998), p. 327.

[32] Z. Yu, P. Deshpande, W. Wu, J. Wang, and S. Y. Chou, Reflective polarizer based on a stacked double-layer subwavelength metal grating structure fabricated using nanoimprint lithography, Appl. Phys. Lett. **77**, 927 (2000).

[33] T. Doumuki and H. Tamada, An aluminum-wire grid polarizer fabricated on a gallium-arsenide photodiode, Appl. Phys. Lett. **71**, 686 (1997).

[34] X. J. Yu and H. S. Kwok, Optical wire-grid polarizers at oblique angles of incidence, J. Appl. Phys. **93**, 4407 (2003).

[35] S. Y. Chou and W. Deng, Subwavelength amorphous silicon transmission gratings and applications in polarizers and waveplates, Appl. Phys. Lett. **67**, 742 (1995).

[36] B. C. Cullity and S. R. Stock, *Elements of X-Ray Diffraction*, 3rd ed. (Addison-Wesley, Reading, Massachusetts, 1956), p. 105.

[37] X. R. Huang, R. W. Peng, Z. Wang, F. Gao, and S. S Jiang, Charge-oscillation-induced light transmission through subwavelength slits and holes, Phys. Rev. A **76**, 035802 (2007).

[38] X. Huang and R. Peng, General mechanism involved in subwavelength optics of conducting microstructures: Charge-oscillation-induced light emission and interference, J. Opt. Soc. Am. A **27**, 718 (2010).

[39] M. N. Polyanskiy, "Refractive index database", https://refractiveindex.info.

[40] G. S. Krinchik and V. A. Artemjev, Magneto-optic properties of Nickel, Iron, and Cobalt, J. Appl. Phys. **39**, 1276 (1968).